Published in final edited form as:
Nat Nanotechnol. 2009 November ; 4(11): 773–780. doi:10.1038/nnano.2009.294.

A route to brightly fluorescent carbon nanotubes for near-infrared imaging in mice

Kevin Welsher[1], **Zhuang Liu**[1,2], **Sarah P. Sherlock**[1], **Joshua Tucker Robinson**[1], **Zhuo Chen**[1], **Dan Daranciang**[1], and **Hongjie Dai**[1,*]

[1]Department of Chemistry, Stanford University, Stanford, California 94305, USA

[2]Functional Nano & Soft Materials (FUNSOM) Laboratory, Soochow University, Suzhou, Jiangsu, 215123, China

Abstract

The near-infrared photoluminescence intrinsic to semiconducting single-walled carbon nanotubes is ideal for biological imaging owing to the low autofluorescence and deep tissue penetration in the near-infrared region beyond 1 μm. However, biocompatible single-walled carbon nanotubes with high quantum yield have been elusive. Here, we show that sonicating single-walled carbon nanotubes with sodium cholate, followed by surfactant exchange to form phospholipid–polyethylene glycol coated nanotubes, produces *in vivo* imaging agents that are both bright and biocompatible. The exchange procedure is better than directly sonicating the tubes with the phospholipid–polyethylene glycol, because it results in less damage to the nanotubes and improves the quantum yield. We show whole-animal *in vivo* imaging using an InGaAs camera in the 1–1.7 μm spectral range by detecting the intrinsic near-infrared photoluminescence of the 'exchange' single-walled carbon nanotubes at a low dose (17 mg l^{-1} injected dose). The deep tissue penetration and low autofluorescence background allowed high-resolution intravital microscopy imaging of tumour vessels beneath thick skin.

Single-walled carbon nanotubes (SWNTs) have shown potential for biological and medical[1] applications because of their intrinsic optical properties and ability to load both targeting ligands and chemotherapy drugs, *in vitro*[2,3] and *in vivo*[4–6]. Their unique optical properties make SWNTs attractive candidates for biological imaging[7–11] and sensing[12]. In particular, the near-infrared (NIR) photoluminescence of semiconducting SWNTs[13] has made them promising as NIR fluorescent contrast agents in biological systems[8–11]. SWNT NIR fluorescent probes with emission mostly in the infrared-A (IR-A, 1–1.4 μm) region (Fig. 1) are ideal as biological probes because of the inherently low autofluorescence in the NIR range (0.8–1.7 μm)[14] and large Stokes shift between the excitation and emission bands, which allows excitation in the biological transparency window[15] near 800 nm while further reducing the background effects of autofluorescence and scattering. Work carried out by Lim and colleagues[16] has predicted that NIR fluorophores with emission in the 1,100–1,400 nm range have higher tissue penetration than those near 800 nm by considering the

* Correspondence and requests for materials should be addressed to H.D. hdai@stanford.edu.

Author contributions

K.W., Z.L., S.S., J.R., D.D. and H.D. conceived and designed the experiments. K.W., Z.L., S.S., J.R. and Z.C. performed the experiments. K.W. analysed the data. K.W. and H.D. co-wrote the paper.

Additional information

Supplementary information accompanies this paper at www.nature.com/naturenanotechnology. Reprints and permission information is available online at http://npg.nature.com/reprintsandpermissions/.

wavelength-dependent scatter by tissue. Nanotubes provide a unique way in which to probe this advantageous emission region. However, whole-animal *in vivo* NIR photoluminescence imaging has yet to be achieved using SWNTs because of several stumbling blocks that need to be overcome.

The biggest challenge in realizing SWNT NIR probes is the development of bright SWNTs with high biocompatibility. The use of SWNTs *in vivo* requires appropriate functionalization to reduce toxicity and non-specific binding. We have developed the use of phospholipid–polyethylene glycol (PL–PEG) moieties for the suspension of SWNTs in aqueous media[17]. The phospholipid binds to the nanotube surface by means of hydrophobic interactions, and the PEG chain imparts water solubility and biocompatibility. SWNTs functionalized in this way are exceptionally stable and can remain in serum at up to 70 °C for months. PL–PEG functionalized nanotubes have been shown to be non-toxic *in vitro* and *in vivo* and are excreted over time5,6. Unfortunately, SWNTs directly sonicated in PL–PEG over long periods (≥15 min) have relatively low quantum yield when compared with those suspended in non-biocompatible surfactants such as the bile salt sodium cholate[18] (Fig. 1). This loss of quantum yield is not ideal for biological imaging where sensitivity is imperative.

In this work, we first debundled and solubilized pristine SWNTs in sodium cholate, then displaced the sodium cholate with a PL– PEG group. The resulting SWNT solutions demonstrated an increase in relative quantum yield of more than one order of magnitude compared to SWNTs directly dispersed in PL–PEG, while still maintaining the high biocompatibility that is characteristic of SWNTs functionalized by PL–PEG (Supplementary Fig. S1). The NIR photoluminescence emission was used to perform targeted cell imaging. Furthermore, for the first time, whole-animal NIR photoluminescence imaging of SWNTs was achieved using an InGaAs camera, at a dose 10 times lower than would be required when using SWNTs directly suspended in PL–PEG. Importantly, a near-zero autofluorescence background was observed in the SWNT emission range (1,100–1,700 nm). These exchange-SWNTs also made possible high-resolution intravital tumour vessel imaging through thick skin in a live mouse.

Preparation and characterization of exchange-SWNTs

Cholate–SWNT suspensions were prepared as described in the literature13,18,19. Briefly, 1 mg of raw HiPCO SWNTs (Carbon Nanotechnologies) and 40 mg of sodium cholate were added to 4 ml of water. The mixture was bath sonicated for 1–6 h. The resulting black suspension was ultracentrifuged at 300,000*g* for 1 h to remove large aggregates and bundled nanotubes, leaving a dark suspension of predominantly single SWNTs. To this suspension was added 1 mg ml^{-1} of DSPE–$mPEG_{5k}$ (1,2-distearoyl-*sn*-glycero-3-phosphoethanolamine–*N*-[methoxy(polyethylene glycol)5000], Laysan Bio), followed by brief sonication (<1 min) to ensure that the DSPE–$mPEG_{5k}$ was fully dissolved. The solution was then dialysed against a 3,500 MWCO (molecular weight cut-off) membrane over a period of 4–5 days with multiple water changes per day. This process slowly removes the sodium cholate from the solution, allowing the DSPE–$mPEG_{5k}$ to coordinate to the surface of the nanotubes. Following dialysis, the solution was again ultracentrifuged (300,000*g*, 1 h) to remove any bundles that may have formed during the exchange process, resulting in the exchange-SWNTs. For direct-SWNT/DSPE–$mPEG_{5k}$ conjugates, 0.25 mg ml^{-1} of raw HiPCO product was bath sonicated in 1 mg ml^{-1} of DSPE–$mPEG_{5k}$ for 1 h, followed by ultracentrifugation to obtain the supernatant.

Figure 1c plots the photoluminescence versus excitation spectra for cholate–SWNT, exchange-SWNT and direct-SWNT suspensions. To compare the relative quantum yield of each of the samples, the photoluminescence spectrum (900–1,500 nm) at 650 nm excitation

was integrated for each sample and normalized to the cholate–SWNT value. The exchange-SWNTs were able to maintain the high photoluminescence yield of the cholate suspended nanotubes, exhibiting a relative quantum yield of 0.84 compared to cholate–SWNT. Direct tubes, however, presented a relative quantum yield of only 0.03. On average, exchange-SWNTs show a 15-fold advantage in quantum yield over direct-SWNTs. The small drop in quantum yield between the cholate and exchange samples is probably due to bundling occurring during the exchange process that is not removed by the centrifuge step. However, this drop is minor compared to the low relative quantum yield of the direct-SWNT sample. Because both the exchange-SWNT and direct-SWNT samples are subject to the same centrifuge conditions, it is unlikely that the large difference in quantum yield observed is due to the presence of nanotube bundles.

Inspection of the UV–vis–NIR spectra (Cary 6000i) (Fig. 1d) reveals a marked difference in the absorption peaks of the cholate, exchange and direct samples, particularly in the 1,000–1,300 nm range corresponding to first van Hove singularities (E_{11}). The cholate and exchange samples, which have high relative quantum yields, present sharp E_{11} absorption peaks (1,000–1,300 nm, Fig. 1d), but the direct sample, which has a low relative quantum yield, has short, broad E_{11} absorption peaks. As a result, the peak sharpness is seen to correlate directly with the relative quantum yield.

Further investigation of the UV–vis–NIR spectra for the cholate– SWNT and the exchange-SWNT suspensions shows that the E_{11} peaks of the exchange sample are slightly redshifted relative to those of the cholate samples (Fig. 1d). This redshift can also been seen in the photoluminescence versus excitation spectra of Fig. 1c. These peak shifts in the absorption and emission spectra are probably evidence of surfactant exchange. Many reports in the literature[19,20] demonstrate that the exposure of the nanotube sidewall to polar molecules such as water leads to a reduced optical bandgap owing to dielectric screening, resulting in redshifted peaks in the optical absorption spectra and photoluminescence versus excitation spectra. We suggest that cholate forms a more complete coating on the nanotube in its micelle form, whereas the PL–PEG still allows some water to reach the nanotube surface. In fact, the ability of molecules to reach the surface of a nanotube suspended in PL–PEG has been used to load the chemotherapy agent doxorubicin to the nanotube sidewall through π–π stacking[21]. This exposed surface allows screening by the solvent molecules, resulting in redshifted spectral peaks.

It is worth noting that the photoluminescence versus excitation spectra of the two samples also show variations in the relative photoluminescence intensity of different chirality nanotubes (Fig. 1c). The difference in brightness of certain nanotube chiralities between the cholate–SWNT and exchange-SWNT samples is probably a symptom of a bias that each surfactant coating has for a certain diameter of nanotube. The photoluminescence versus excitation data suggest that cholate may prefer smaller-diameter nanotubes (larger bandgap), whereas the PL–PEG prefers larger-diameter nanotubes (smaller bandgap). During the exchange process, the PL–PEG may be slightly more likely to wrap around a larger-diameter nanotube, leading to a higher fraction of those tubes in the exchange-SWNT product.

Examination of atomic force microscopy (AFM) images (Fig. 2a,b) found that the exchange-SWNTs were longer, on average, than direct-SWNTs (Fig. 2c). The exchange-SWNTs ranged from 50 nm to over 1.8 μm in length, with an average of ~372 ± 310 nm. The direct-SWNTs ranged from 50 nm to 450 nm in length, with an average of ~161 ± 85 nm. In each case, 75 nanotubes were counted. This observed length difference is a likely contributor to the reduction in quantum yield, previous work having shown that length can have an effect on nanotube photoluminescence quantum yield22. This loss of quantum yield is probably a

result of the fact that the diffusion length of an exciton in an SWNT is of the order of 100 nm (refs 23,24). If we consider the ends of the nanotube to contain defects that completely quench the excitons before they can radiatively decay, then it is expected that an exciton in 100-nm-long SWNT has a much smaller chance of emitting a photon than an exciton in a 1-μm-long SWNT. However, because the average lengths of the direct and exchange samples differed only by a factor of two, and the quantum yield differed by more than one order of magnitude, it is likely that length is not the only factor and defects exist along the sidewalls of direct-SWNTs.

Raman spectroscopy was used to assess the quality of SWNT structure for the three different species. By comparing the ratio of the G band (proportional to the number of sp^2 carbon sites, ~1,600 cm^{-1}) to the D band (a measure of the defects in a nanotube sample, ~1,300 cm^{-1})[25] it was possible to determine a semi-quantitative estimate of how pristine the nanotube structure was (Fig. 2d). It can be seen that the direct sample has the highest D band, and the cholate and exchange samples have lower and relatively similar D-band intensities. The high D/G ratio for direct-SWNTs indicates a higher population of defects, probably on the nanotube sidewall. This indicates that the SWNTs directly sonicated in PL–PEG are less pristine than those sonicated in sodium cholate. A higher density of sidewall defects would significantly reduce the radiative lifetime of an exciton, leading to a loss of quantum yield.

We propose that exchange-SWNTs are more pristine than direct-SWNTs because long periods of sonication in PL–PEG lead to the creation of sidewall defects. By avoiding long sonication in PL–PEG, the integrity of the SWNT sidewall can be maintained. The AFM data (Fig. 2a–c) support the idea that SWNTs are damaged by direct sonication in PL–PEG. The reduction in SWNT length is probably initially due to the formation of defects at the SWNT sidewall followed by cutting at that defect site. The Raman spectra (Fig. 2d) further indicate that the direct-SWNTs contain more defects than the exchange-and cholate–SWNTs. To confirm that the creation of defects and low quantum yield in SWNTs directly suspended in PL–PEG is a consequence of the presence of PL–PEG during sonication, exchange-SWNTs (excess cholate removed by means of dialysis) were sonicated for 1, 15 and 60 min. The UV–vis–NIR, photoluminescence versus excitation, Raman (Supplementary Fig. S2) and AFM (Supplementary Fig. S3) data all indicate that long periods of sonication in PL–PEG lead to the creation of defects and the eventual cutting of the tubes, probably at the defect sites. The creation of defect sites, both at the tube ends and on the sidewall, both contribute to the loss of quantum yield observed in SWNTs sonicated in the presence of PL–PEG. It should be noted that the UV–vis–NIR peaks (Supplementary Fig. S2a) show a decrease in peak sharpness with increasing sonication time, similar to that seen in Fig. 1d. We propose that the UV–vis–NIR peak sharpness decreases with increasing density of sidewall defects and can be used as an easy measure of the integrity of the SWNT sidewall.

At this point, the mechanism of this PL–PEG induced cutting and defect creation of SWNTs during sonication is unclear. Sonication of SWNTs in excess cholate alone (Supplementary Fig. S4) or in the presence of 5 kDa PEG (Supplementary Fig. S5) had no effect on the integrity of the nanotube structure, even for long sonication periods of up to 6 h. A control experiment using a non-phosphate-containing amphiphile (ceramide–$mPEG_{750}$) showed that the phosphate group is not a critical factor in nanotube sidewall defect formation (Supplementary Fig. S6a,b). Further experiments showed that the presence (or absence) of atmospheric oxygen is also not critical to the cutting process and low quantum yield of direct-SWNTs (Supplementary Fig. S6c). Determining the mechanism of defect creation in direct-SWNTs in future work will be critical to the development of SWNT conjugates for bio-imaging.

In vitro and *in vivo* imaging

To prove the utility of these bright, biocompatible SWNTs, targeted cell imaging was carried out in the 1,100–1,700 nm range using the intrinsic NIR photoluminescence of the exchange-SWNTs (Fig. 3). To add functionality, SWNTs were exchanged into a mixture of 25% DSPE–PEG_{5k}–NH_2 and 75% DSPE–$mPEG_{5k}$ as described above. For cell targeting, an arginine–glycine–aspartic acid (RGD) peptide ligand was linked to the amine residue on the PEG chain by means of succinimidyl-4-(*N*-maleimidomethyl)cyclohexane-1-carboxylate (SMCC) chemistry (see Methods) to selectively bind to $\alpha_v\beta_3$-integrin positive cells[5]. The $\alpha_v\beta_3$-integrin positive U87 MG cell line treated with the exchange-SWNT/RGD conjugate (Fig. 3a) shows a high, uniform NIR photoluminescence signal (green), whereas the $\alpha_v\beta_3$-integrin-negative MDA-MB-468 cell line (Fig. 3b) does not. This indicates that the RGD is successfully bound to the exchange-SWNTs and that the non-specific binding to non-targeted cells is low, an indicator of a biologically inert surface coating. Furthermore, both the positive and negative cell lines treated with direct-SWNT/RGD (Fig. 3c,d) at the same concentration show much lower photoluminescence signal than U87 cells treated with the exchange-SWNTs. Low cell autofluorescence is seen for all samples. The high quantum yield of exchange-SWNTs has clearly facilitated NIR imaging of cells *in vitro*.

To further explore the use of the exchange-SWNT conjugates, we used both the exchange- and direct-SWNT varieties to perform *in vivo* NIR photoluminescence imaging in mice. Nude mice were injected with 260 mg l^{-1} (200 μl) of direct-SWNT/DSPE–$mPEG_{5k}$ and 17 mg l^{-1} (200 μl) of exchange-SWNTs in phosphate-buffered saline (PBS), respectively. Nanotube weight concentrations were determined using an extinction coefficient of 46.5 (wt % in mg $l^{-1})^{-1}$ cm^{-1} at 808 nm as derived by Kam and colleagues[17]. NIR photoluminescence images were taken 30 min and 24 h following intravenous injection (Fig. 4a–f). Despite the fact that the exchange-SWNT tubes were injected at a 15 times lower dose (Fig. 4a,d, insets), they still show a stronger NIR photoluminescence signal (red) and better contrast than the direct-SWNT-treated mice. The NIR photoluminescence signal shows good tissue penetration, with clear images of SWNTs circulating in the vasculature under the skin (Fig. 4b). Signal from organs deeper inside the mouse can also be seen. This signal is presumably from the liver and spleen, which have been found to be active in removing SWNTs from the blood[6]. Over time, the NIR photoluminescence signal fades for both mice, likely due to the clearance of SWNTs from the body through the reticuloendothelial system (RES). Importantly, the advantage of using NIR photoluminescence for *in vivo* imaging can be seen when an untreated mouse is imaged under the same conditions (Fig. 4g). The autofluorescence level is extremely low in the NIR region beyond 1 μm relative to the signal from the SWNT samples, avoiding the need for special treatment of the autofluorescence background, as must often be carried out in the visible range.

An important feature of the bright exchange-SWNTs over direct-SWNTs is the ability to obtain high-resolution intravital imaging of vessels below the skin of the mice. For imaging, LS174T tumourbearing mice were injected with a relatively high dose of exchange-SWNTs (~170 mg l^{-1}, 300 μl) to ensure a good signal to noise ratio. High-magnification (×50) images were taken up to 90 min post-injection. The images (Fig. 5) show that very small vessels can be resolved to a few micrometres inside the tumour on the shoulder of mice, beneath the relatively thick shoulder skin of the animal, without the use of a dorsal skinfold chamber26 or surgical imaging window[27], despite the low resolution of the camera used (320 × 256 pixels). This type of imaging in the NIR range could be important in monitoring tumour angiogenesis[28] without interference from tissue autofluorescence. Furthermore, even when the same area is imaged for minutes at a time, no loss of signal is seen owing to photobleaching, a common problem with normal fluorescent probes, giving exchange-

SWNTs the ability to monitor vessels continuously for long periods of time without losing photoluminescence yield.

Conclusion

In this work, we combined the high relative quantum yield of SWNTs dispersed in sodium cholate with the biocompatibility of SWNTs dispersed in PL–PEG. These exchange-SWNTs show more than one order of magnitude improvement in relative quantum yield compared to SWNTs directly suspended in PL–PEG. This improvement is attributed to the more pristine nature of the exchange-SWNTs, as made evident by their greater length and smaller Raman D peak. It was also observed that PL–PEG leads to the creation of defects and loss of relative quantum yield, although the chemical mechanism of this change is still unknown. These exchange-SWNT conjugates were then used as a NIR photoluminescence contrast agent for targeted cell imaging and as *in vivo* NIR photoluminescence imaging agents in live mice. Exchange- SWNTs demonstrated the ability to achieve high image contrast at a relatively low dose (17 mg l^{-1}) for whole-mouse imaging. Furthermore, high-magnification NIR photoluminescence imaging was performed on tumour-bearing mice, showing the ability to resolve small vessels inside the tumour. Given their previously demonstrated low toxicity and RES excretion[5,6], this work establishes the use of bright biocompatible SWNTs as versatile *in vivo* NIR photoluminescence imaging agents for live animals.

Whole-animal NIR imaging *in vivo* in the 1,100–1,700 nm range using an InGaAs camera has not been achieved previously with any other agents, including quantum dots and dye molecules. As suggested by Lim and colleagues[16], imaging in this spectral region affords deep tissue penetration. This fact, in combination with the ultralow background autofluorescence in the emission range, makes bright, biocompatible nanotube fluorophores promising biological imaging agents.

Methods

Photoluminescence versus excitation spectra (PLE)

PLE spectra were taken using a homebuilt NIR spectroscopy setup. The excitation source was a 150 W ozone-free xenon lamp (Oriel), which was dispersed by a monochromator (Oriel) to produce excitation lines with a bandwidth of 15 nm. The excitation light was focused onto a 1-mm quartz cuvette containing the sample. Emission was collected in a transmission geometry. The excitation light was rejected using an 850-nm long-pass filter (Omega). The emitted light was directed into a spectrometer (Acton SP2300i) equipped with a liquid-nitrogen-cooled InGaAs linear array detector (Princeton OMA-V). Spectra were corrected post-collection to account for the sensitivity of the detector and the power of the excitation.

Atomic force microscopy

All AFM images were taken in the tapping mode using a Digital Instruments Nanoscope. Samples were prepared by briefly soaking a piece of silicon in the sample, followed by calcination at 300 °C for 20 min to eliminate any excess surfactant.

Raman spectroscopy

Samples for Raman spectroscopy were prepared by drying a drop of the desired sample on a quartz slide. A 785-nm laser diode (Renishaw) was used for excitation.

Near-infrared photoluminescence whole-animal imaging

NIR photoluminescence images were collected using a liquid-nitrogen-cooled, 320 × 256 pixel, two-dimensional InGaAs array (Princeton Instruments) with a sensitivity ranging from 800 to 1,700 nm. The samples were excited using a 20 W808 nm fibre-coupled diode laser (RPMC Lasers). The excitation power density at the imaging plane was ~0.13 W cm^{-2} with a total excitation power of ~8 W. An effort was made to minimize exposure to the excitation by shuttering the excitation light, thereby only exposing the subject for the duration of the camera exposure, which ranged from 10 ms to 1 s. The excitation light was filtered out using a 1,100-nm long-pass filter (Omega) so that the intensity of each pixel represented light in the 1,100–1,700 nm range.

High-magnification near-infrared photoluminescence imaging

Cell and high-magnification intravital imaging were carried out in epifluorescence mode with a 658-nm laser diode (100 mW, Hitachi) focused to a ~100 mm diameter spot by focusing the laser near the back focal length of a ×50 objective lens (Nikon). The resulting NIR photoluminescence was collected using the two-dimensional InGaAs camera. The collected light was filtered as described for the whole-animal imaging case. For cell imaging, exposure times of 1–3 s were used for best signal-to-noise ratio. To account for the breathing of the mouse during intravital tumour vessel imaging, consecutive images (exposure time 1 s) were collected, and the image closest to the focus was chosen for presentation. Images were flat-field-corrected to account for non-uniform laser excitation.

Cell culture and tumour inoculation

All culture media were supplemented with 10% fetal bovine serum, 100 IU ml^{-1} penicillin, 100 μg ml^{-1} streptomycin and L-glutamine. U87 MG cells were cultured in Dulbecco's Modified Eagle Medium (DMEM), with 1 g l^{-1} D-glucose and 110 mg l^{-1} sodium pyruvate. MDA-MB-468 cells were cultured in Leibovitz's L-15 Medium. LS174T cells were cultured in Minimum Essential Medium (MEM) with Earle's Salts, and further supplemented with 1% non-essential amino acids and 1 mM sodium pyruvate. Cells were maintained in a 37 °C incubator with 5% CO_2.

RGD conjugation and cell incubation

Conjugation of RGD peptide to DSPE–PEG_{5k}–NH_2 functionalized SWNTs was carried out following our previously published protocol[5]. Briefly, a SWNT solution at 300 nM after removal of excess DSPE–PEG was mixed with 1 mM sulpho-SMCC at pH 7.4 for 2 h. After removing excess sulpho-SMCC by filtration through 10-kDa filters, RGD-SH was added together with tris(2-carboxyethyl)phosphine (TCEP) at pH 7.4. The final concentrations of SWNT, RGD-SH and TCEP were 300 nM, 0.1 mM and 1 mM, respectively. The reaction was allowed to proceed for 2 days before purification to remove excess RGD and TCEP reagents by filtration through 10-kDa filters. The SWNT/RGD conjugates were then incubated with both an $\alpha_v\beta_3$-positive (U87 MG) and an $\alpha_v\beta_3$-negative (MDA-MB-486) cell line at 4 °C for 1 h. Incubation was at a low temperature to minimize the effect of endocytosis. After incubation, cells were collected by centrifugation and washed with PBS to remove excess SWNTs. The cells were then deposited on a slide at a high density, creating a monolayer of cells in the field of view.

Mouse handling and injection

Athymic nude mice obtained from Harlan Sprague Dawley were housed at Stanford Research Animal Facility (RAF) under Stanford Institutional Animal Care and Use Committee (IACUC) protocols. SWNTs were centrifuged at 10,000*g* for 10 min to remove any possible aggregates before tail-vein injection. During imaging, mice were anaesthetized

by inhalation of 2% isoflurane with oxygen. For inoculation of LS174T tumours, ~2×10^6 cells were implanted subcutaneously on the shoulder of nude mice.

Acknowledgments

The authors would like to thank X. Chen for the RGD peptide. This work was supported partially by CCNE-TR at Stanford University, NIH-NCI RO1 CA135109-02 and Ensysce.

References

1. Liu Z, Tabakman S, Welsher K, Dai H. Carbon nanotubes in biology and medicine: *in vitro* and *in vivo* detection, imaging and drug delivery. Nano Res 2009;2:85–175. [PubMed: 20174481]
2. Dhar S, et al. Targeted single-wall carbon nanotube-mediated Pt(IV) prodrug delivery using folate as a homing device. J. Am. Chem. Soc 2008;130:11467–11476. [PubMed: 18661990]
3. Liu Z, Winters M, Holodniy M, Dai HJ. siRNA delivery into human T cells and primary cells with carbon-nanotube transporters. Angew Chem. Int. Ed 2007;46:2023–2027.
4. Liu Z, et al. Drug delivery with carbon nanotubes for *in vivo* cancer treatment. Cancer Res 2008;68:6652–6660. [PubMed: 18701489]
5. Liu Z, et al. *In vivo* biodistribution and highly efficient tumour targeting of carbon nanotubes in mice. Nature Nanotech 2007;2:47–52.
6. Liu Z, et al. Circulation and long-term fate of functionalized, biocompatible single-walled carbon nanotubes in mice probed by Raman spectroscopy. Proc. Natl Acad. Sci. USA 2008;105:1410–1415. [PubMed: 18230737]
7. De La Zerda A, et al. Carbon nanotubes as photoacoustic molecular imaging agents in living mice. Nature Nanotech 2008;3:557–562.
8. Cherukuri P, Bachilo SM, Litovsky SH, Weisman RB. Near-infrared fluorescence microscopy of single-walled carbon nanotubes in phagocytic cells. J. Am. Chem. Soc 2004;126:15638–15639. [PubMed: 15571374]
9. Cherukuri P, et al. Mammalian pharmacokinetics of carbon nanotubes using intrinsic near-infrared fluorescence. Proc. Natl Acad. Sci. USA 2006;103:18882–18886. [PubMed: 17135351]
10. Leeuw TK, et al. Single-walled carbon nanotubes in the intact organism: near-IR imaging and biocompatibility studies in Drosophila. Nano Lett 2007;7:2650–2654. [PubMed: 17696559]
11. Welsher K, Liu Z, Daranciang D, Dai H. Selective probing and imaging of cells with single walled carbon nanotubes as near-infrared fluorescent molecules. Nano Lett 2008;8:586–590. [PubMed: 18197719]
12. Chen Z, et al. Protein microarrays with carbon nanotubes as multicolor Raman labels. Nature Biotechnol 2008;26:1285–1292. [PubMed: 18953353]
13. O'Connell MJ. Band gap fluorescence from individual single-walled carbon nanotubes. Science 2002;297:593–596. [PubMed: 12142535]
14. Aubin JE. Autofluorescence of viable cultured mammalian cells. J. Histochem. Cytochem 1979;27:36–43. [PubMed: 220325]
15. Britton C, et al. Near-infrared images using continuous, phase-modulated, and pulsed light with quantitation of blood and blood oxygenation. Ann. NY Acad. Sci 1998;838:29–45. [PubMed: 9511793]
16. Lim YT, et al. Selection of quantum dot wavelengths for biomedical assays and imaging. Mol. Imag 2003;2:50–64.
17. Kam NWS, O'Connell M, Wisdom JA, Dai H. Carbon nanotubes as multifunctional biological transporters and near-infrared agents for selective cancer cell destruction. Proc. Natl Acad. Sci. USA 2005;102:11600–11605. [PubMed: 16087878]
18. Wenseleers W, et al. Efficient isolation and solubilization of pristine single-walled nanotubes in bile salt micelles. Adv. Funct. Mater 2004;14:1105–1112.
19. Hertel T, et al. Spectroscopy of single- and double-wall carbon nanotubes in different environments. Nano Lett 2005;5:511–514. [PubMed: 15755104]

20. Chiashi S, Watanabe S, Hanashima T, Homma Y. Influence of gas adsorption on optical transition energies of single-walled carbon nanotubes. Nano Lett 2008;8:3097–3101. [PubMed: 18759486]
21. Liu Z, Sun X, Nakayama-Ratchford N, Dai H. Supramolecular chemistry on water-soluble carbon nanotubes for drug loading and delivery. ACS Nano 2007;1:50–56. [PubMed: 19203129]
22. Heller DA, et al. Concomitant length and diameter separation of single-walled carbon nanotubes. J. Am. Chem. Soc 2004;126:14567–14573. [PubMed: 15521777]
23. Cognet L, et al. Stepwise quenching of exciton fluorescence in carbon nanotubes by single-molecule reactions. Science 2007;316:1465–1468. [PubMed: 17556581]
24. Georgi C, et al. Photoinduced luminescence blinking and bleaching in individual single-walled carbon nanotubes. ChemPhysChem 2008;9:1460–1464. [PubMed: 18506857]
25. Saito, R.; Dresselhaus, G.; Dresselhaus, MS. Physical Properties of Carbon Nanotubes. Imperial College Press; 1998.
26. Kedrin D, et al. Intravital imaging of metastatic behavior through a mammary imaging window. Nature Meth 2008;5:1019–1021.
27. Lehr HA, et al. Dorsal skinfold chamber technique for intravital microscopy in nude mice. Am. J. Pathol 1993;143:1055–1062. [PubMed: 7692730]
28. Jain RK, Munn LL, Fukumura D. Dissecting tumour pathophysiology using intravital microscopy. Nature Rev. Canc 2002;2:266–276.

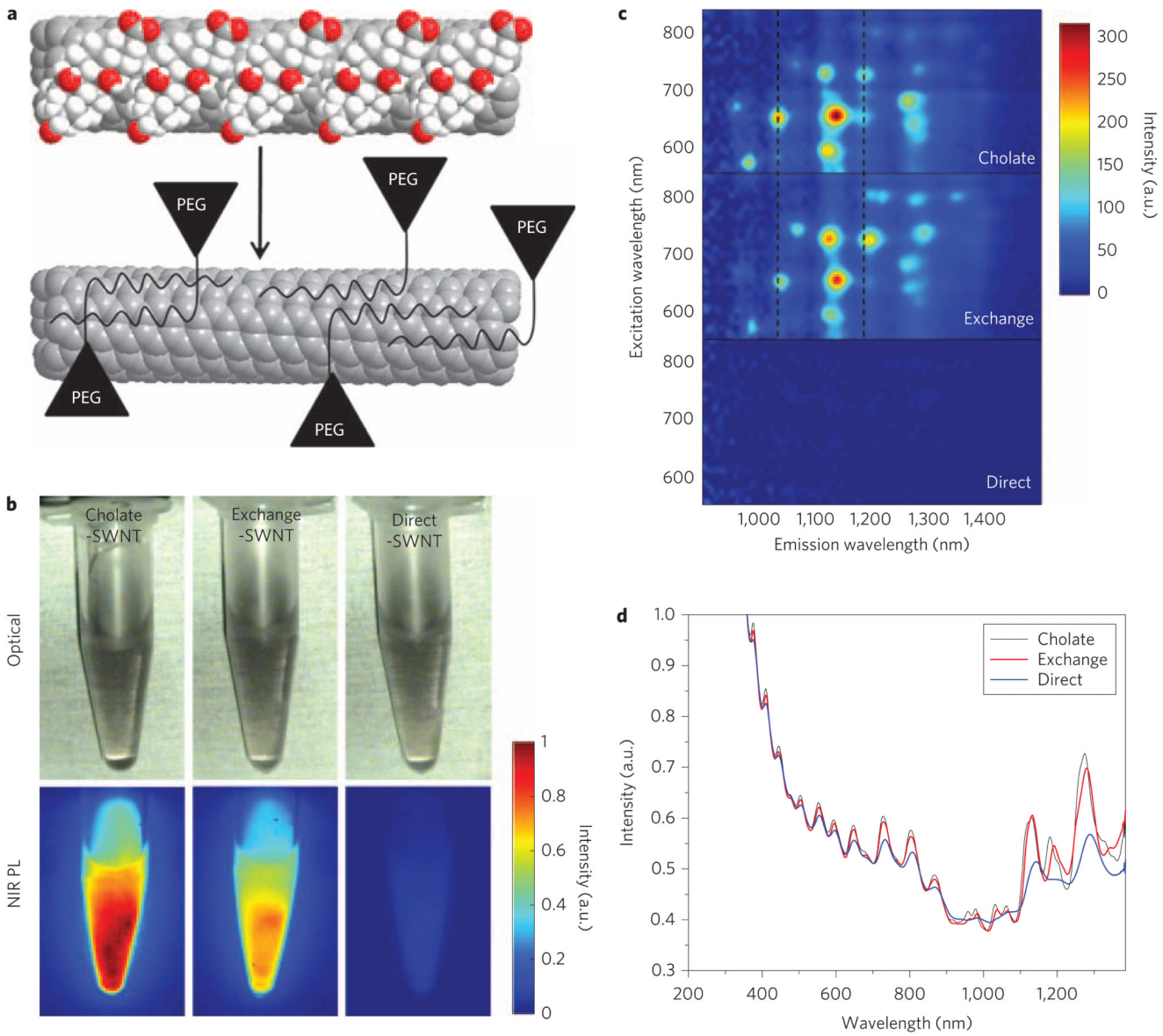

Figure 1. Comparison of exchange- and direct-SWNTs

a, Schematic of the exchange process. Cholate (red and white balls) on SWNTs (grey) is dialysed and eventually replaced by phospholipid–polyethylene glycol (PL–PEG) to form biocompatible nanotubes without damaging the integrity of the nanotube sidewall. **b**, NIR photoluminescence images of the three solutions excited at 808 nm at equal concentrations. Exchange-SWNTs show greater fluorescence yield than direct-SWNTs. **c**, Photoluminescence versus excitation spectra show improved quantum yield in cholate and exchange samples. The dotted lines show how peaks are redshifted after exchange. **d**, UV–vis–NIR curves. Exchange- and cholate-SWNTs show sharp transition peaks; direct-SWNTs show very low and broad absorption features. PL, photoluminescence.

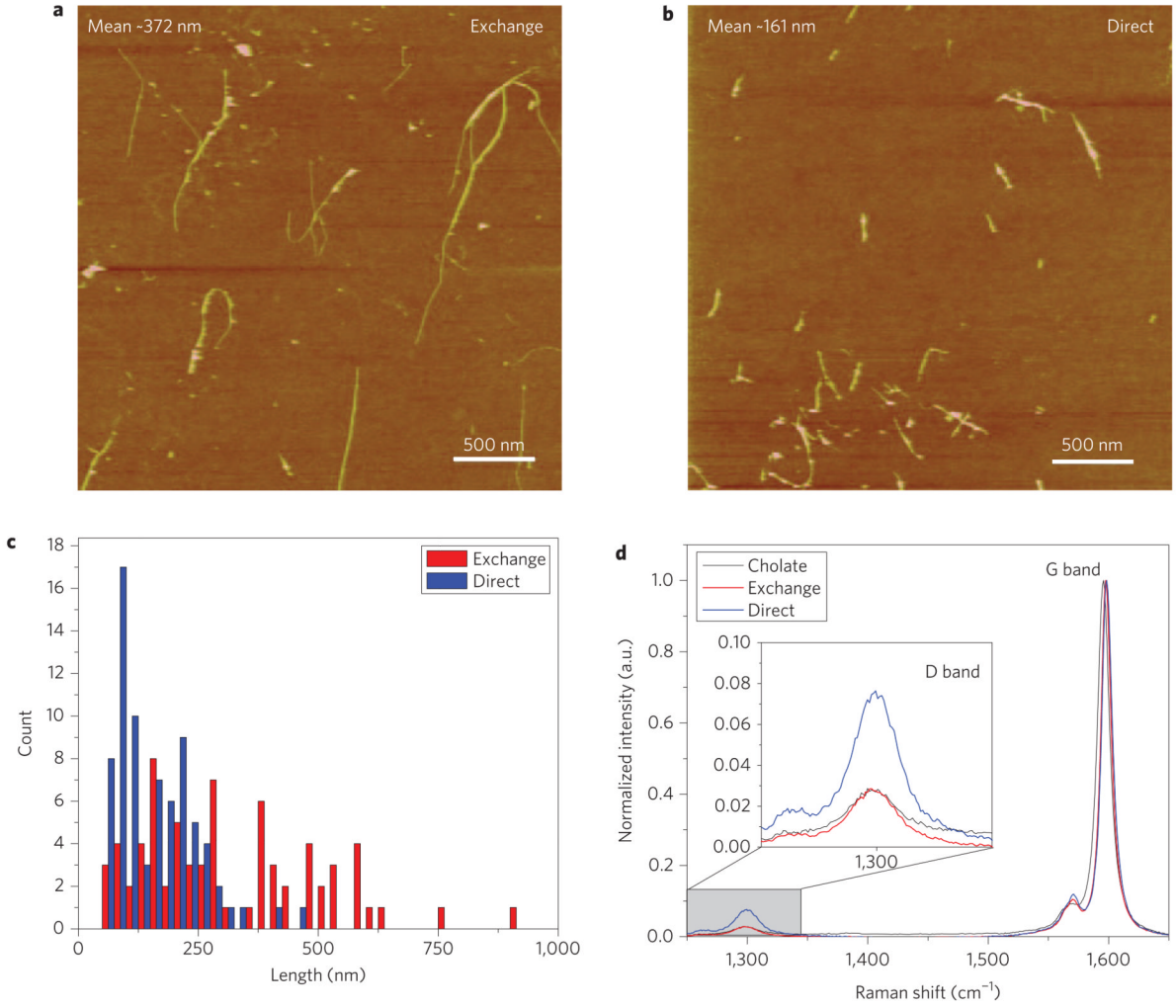

Figure 2. Atomic force microscopy and Raman spectroscopy

a,**b**, AFM topography images of exchange- (**a**) and direct- (**b**) SWNTs. The average lengths of the exchange and direct samples are 372 and 161 nm, respectively. **c**, Histogram of length distributions of exchange and direct samples. The exchange sample has lengths ranging from 50 nm up to 1.8 μm. The direct sample has a narrower distribution, with most SWNTs near 100 nm in length and none longer than 500 nm. **d**, Raman spectra of the three samples. The higher D band in direct-SWNTs indicates a greater number of defects and explains the lower quantum yield.

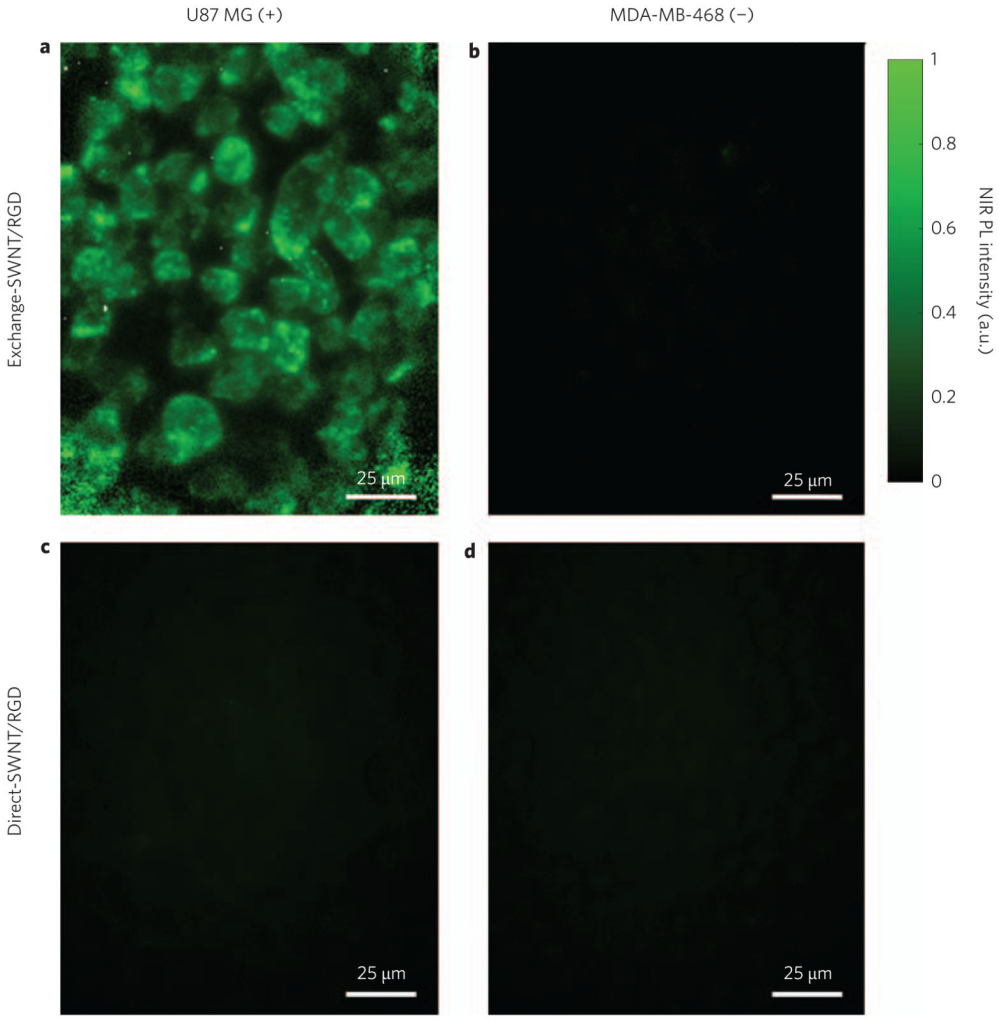

Figure 3. ***In vitro*** **NIR photoluminescence targeted cell imaging**

a–d, NIR photoluminescence images (1,100–1,700 nm) of human malignant glioma cells (U87 MG) treated with exchange-SWNT/RGD (**a**,**b**) and direct-SWNT/RGD (**c**,**d**) conjugates. Arginine–glycine–aspartic acid (RGD) peptide ligand binds to $\alpha_v\beta_3$-integrin overexpressed on the cells. Human breast cancer cell line (MDA-MB-468) is used as a negative. Cells treated with exchange-SWNT/RGD show a high positive signal with very low non-specific binding to the negative cell line. The direct-SWNT/RGD conjugates gave images with very little NIR photoluminescence signal.

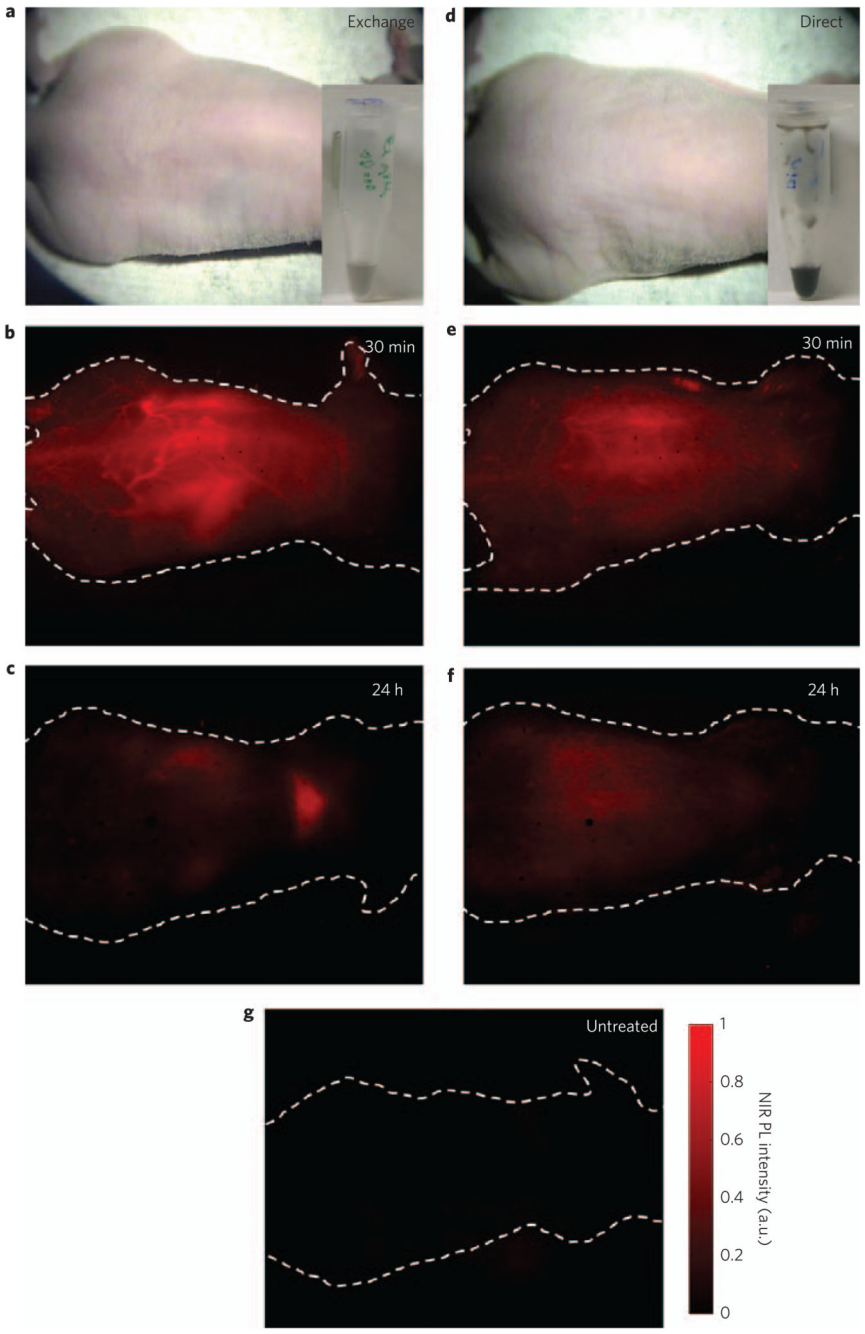

Figure 4. ***In vivo*** **NIR photoluminescence imaging of mice**

a–f, NIR photoluminescence images (1,100–1,700 nm) of nude mice treated with 200 μl of 17 mg l^{-1} exchange-SWNTs (**a–c**) and 200μl of 260mg l^{-1} direct-SWNTs (**d–f**). Solution images show the difference in concentration of the injected doses of the exchange-SWNTs (inset, a) and direct-SWNTs (inset, d). Exchange-SWNTs show high image contrast despite their dose being a factor of 15 lower than that of the direct-SWNTs. Images were taken 30 min (**b**,**e**) and 24 h (**c**,**f**) post tail-vein injection. At early time points, the vasculature beneath the skin is visible as a result of the SWNTs circulating in the blood. The photoluminescence signal from deeper in the mouse is probably due to strong reticuloendothelial system uptake. **g**, NIR photoluminescence image of an untreated nude mouse showing ultralow

autofluorescence. The photoluminescence signal from the SWNTs is easily distinguishable from the endogenous autofluorescence without any image processing. All images used an exposure time of 100 ms.

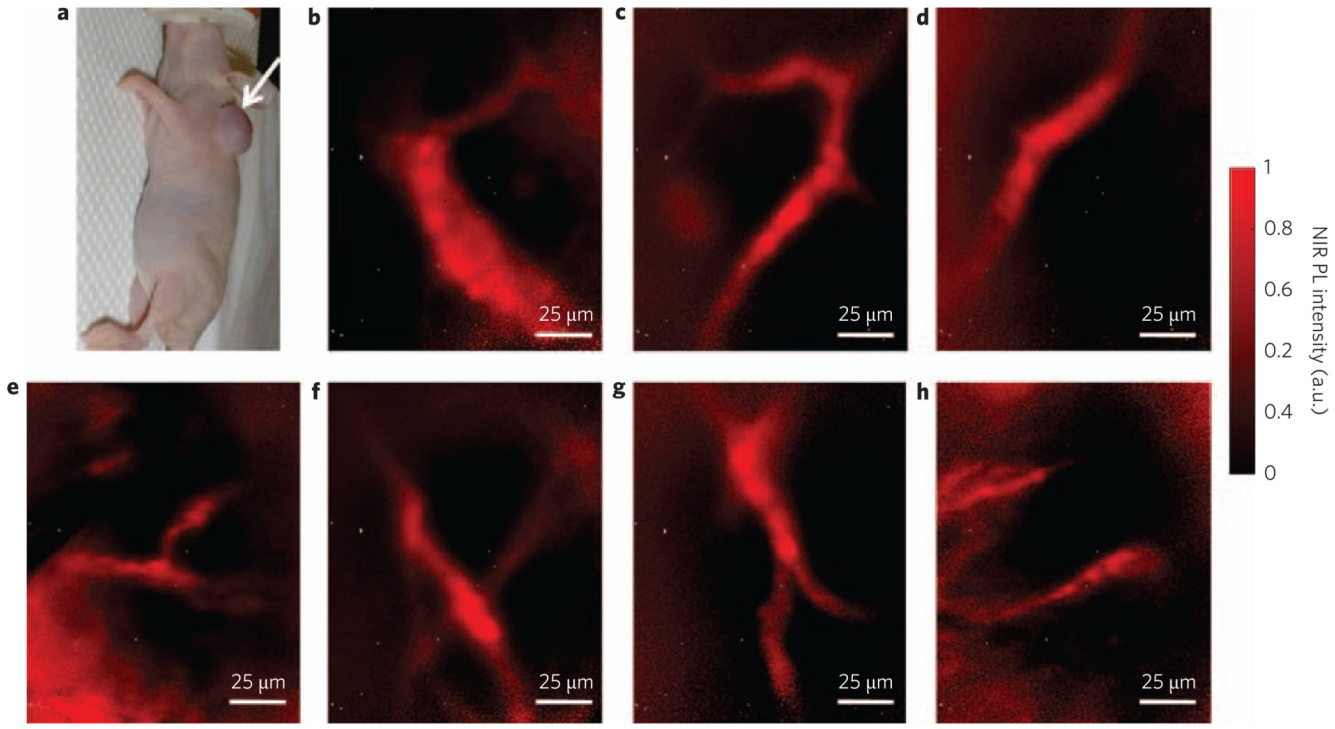

Figure 5. Intravital NIR photoluminescence imaging of tumour vessels

a, Optical image of LS174T tumour-bearing mouse used for intravital microscopy. **b–h**, High-magnification NIR photoluminescence images taken within 90 min of injection of a high concentration (~170 mg l^{-1}, 300μl) of exchange-SWNTs. Tumour vessels can be resolved to a few micrometres, approaching the diffraction limit. Exposure times for all images were 1 s.